Synergistic conversion of CO_2 into C1 and C2 gases using hybrid in-doped TiO_2 and g-C_3N_4 photocatalysts

Jiyeon Park [a,1], Hao Liu [a,1], Guangxia Piao [a], Unseock Kang [a], Hye Won Jeong [b,*], Csaba Janáky [b], Hyunwoong Park [a,*]

[a] *School of Energy Engineering, Kyungpook National University, Daegu 41566, Republic of Korea*
[b] *Department of Physical Chemistry and Materials Science, University of Szeged, Szeged H-6720, Hungary*

A B S T R A C T

Achieving high-efficiency photocatalytic conversion of CO_2 into value-added chemicals remains a challenge. This study synthesizes In-doped TiO_2 and g-C_3N_4 composites (In-TiO_2/g-C_3N_4) via a facile and reliable method. The as-synthesized In-TiO_2/g-C_3N_4 produces CO, CH_4, and C_2H_4 under UV, and CO and CH_4 under visible light from gaseous CO_2 and H_2O vapor. A prolonged photocatalysis results in the continuous production of the same set of carbonaceous compounds over 30 h, with a photonic yield of $\sim$ 40%. The yield of C_2H_4 with In-TiO_2/g-C_3N_4 is $\sim$ 11-times greater than the sum of In-TiO_2 and g-C_3N_4. The CO_2 adsorption isotherms show that In-TiO_2 acts as a CO_2 adsorbent and photocatalyst whereas g-C_3N_4 mainly works as a photocatalyst. In-situ FTIR study reveals the formation of CH_4 and C_2H_4 on In-TiO_2/g-C_3N_4. Time-resolved photoluminescence indicate that In-doping facilitates charge transfer and a strongly coupled g-C_3N_4 induces cascaded charge transfer. This leads to inhibited charge recombination and long-lived charge carriers.

1. Introduction

Over the last few decades, photocatalytic CO_2 conversion has gained popularity as one of the artificial photosynthesis technologies [1–5]. It can upgrade captured CO_2 to value-added chemicals, such as CO, methanol, aliphatic acids, and hydrocarbons, using n-type and p-type semiconductor photocatalysts [6–10]. Despite extensive studies, most photocatalysts still suffer from low selectivity (i.e., mixed carbon products), non-stoichiometric redox reactions (i.e., limited or absent water oxidation reactions), short durability, and poor solar conversion efficiency. Some *p*-type semiconductors demonstrated an exceptionally high solar conversion efficiency of $\sim$ 5% over a month under simulated sunlight, with 100%-selective formic acid production and stoichiometric O_2 evolution in the absence of any sacrificial chemicals and electrical biases [6,11–13].

Among *n*-type semiconductors, TiO_2 has been widely studied as a model material because of its low cost, photochemical stability, and environmentally friendly properties [14–16]. Nevertheless, TiO_2 has several photochemical limitations for driving CO_2 reduction reactions (CO_2 RR), including a wide bandgap, poor charge transfer, and

inefficient charge injection. The first two issues are common for most reduction reactions (e.g., O_2 reduction and H_2 evolution). However, the last is critical, particularly for CO_2 RR because the conduction band (CB) has a significantly lower energy level than the one-electron reduction potential of CO_2 (E° (CO_2/$CO_2^{\bullet-}$) $= -1.97$ V) [5]. Nevertheless, the formation of aliphatic acids and C_1 hydrocarbons at irradiated TiO_2/liquid and TiO_2/gas interfaces indicates that proton-coupled electron transfer (PCET) to adsorbed CO_2 is the dominant process. Furthermore, the presence of $C_{\geq 2}$ hydrocarbons indicates that the adsorbed C_1 intermediates are sufficiently long-lived for C–C coupling.

Many surface modifications (e.g., doping, heterojunction, and coupling with co-catalysts) have been attempted to enhance the photocatalytic activity for CO_2 RR (Table S1). Among them, doping with In^{3+} is effective in creating oxygen vacancies in TiO_2 and reducing the charge recombination process [17]. Furthermore, indium-doping can increase the surface area and enlarge the bandgap (E_g) of TiO_2 [18]. Previous studies showed that the inhibited charge recombination significantly increased CH_4 production with In-doped TiO_2, whereas CO was the sole product with bare TiO_2 [17–19]. Coupling with carbon-based materials (e.g., graphitic carbon derivates, graphene, graphene
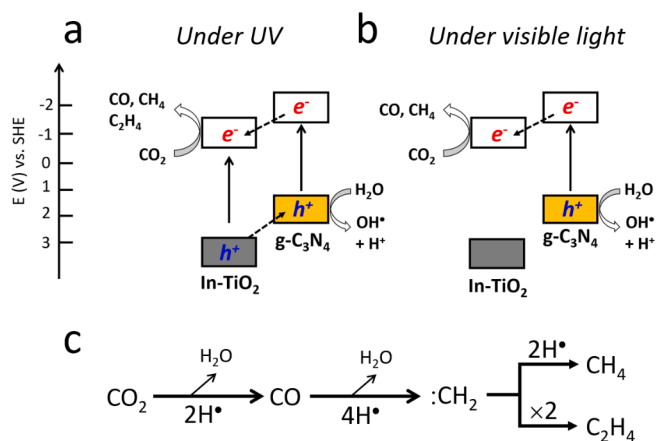
Scheme 1. Schematic illustration of the charge transfer mechanism with In-TiO_2/g-C_3N_4 under (a) UV and (b) visible light. (c) Proposed elementary reaction pathway of photocatalytic CO_2 conversion into CO and hydrocarbons. $H^\bullet$ represents a proton/electron (H^+/e^-) pair.

oxide, and carbon nanotubes) can also improve the TiO_2 activity. The electrically conductive carbon materials with a large surface area can serve as an adsorbent of CO_2 and catalyst of CO_2 RR because of their unique electronic properties [20,21]. Among carbon materials, graphitic carbon nitride (g-C_3N_4) has a semiconductor property with a narrow E_g (~2.7 eV). When coupled to TiO_2, g-C_3N_4 captures visible light ($\lambda \sim 460$ nm) and facilitates photogenerated charge transfer (Scheme 1) [22–24].

Therefore, this study synthesized In-doped TiO_2 and g-C_3N_4 using sol–gel and thermal polymerization processes, respectively, and coupled them using an impregnation method. Considering different E_gs of TiO_2 and g-C_3N_4, the photocatalytic activity of the as-synthesized samples (TiO_2, In-TiO_2, g-C_3N_4, TiO_2/g-C_3N_4, and In-TiO_2/g-C_3N_4) was examined for CO_2 RR under UV ($\lambda = 365$ nm) and visible light ($\lambda > 420$ nm). Particularly, the yield, total charge consumption, and photoelectrochemical features were analyzed, and charge carrier transfer dynamics were examined. Based on the experimental results, photocatalytic reaction mechanisms under UV and visible light were proposed. Finally, the as-synthesized composites were characterized using various surface analysis tools (XRD, XPS, Raman, FTIR, UV–vis absorption, BET, and HR-TEM).

2. Experimental section

2.1. Synthesis of materials

A series of In-TiO_2 samples were synthesized using a sol–gel method. Titanium tetrabutoxide (Ti(C_4H_9O)$_4$, 4.8 mL, Sigma-Aldrich reagent grade, 97%) was added to a vigorously stirred aqueous solution containing *tert*-butanol (12.6 mL, Sigma-Aldrich, ACS reagent, 99.0%), acetic acid (1.4 mL, Sigma-Aldrich, ACS reagent, ≥99.7%), deionized water (18 MΩ cm, 1.2 mL), and various amounts of indium nitrate (In (NO_3)$_3$·$x$$H_2O$, Sigma-Aldrich, 99.9%). The mole fractions of In (In / (Ti + In)) were 0.01–0.15; unless otherwise specified, the mole fraction was fixed to be 0.05. The as-obtained gel was aged for 24 h and dried at 105 °C, followed by calcination at 450 °C in the air for 4 h. g-C_3N_4 was synthesized by thermal polymerization of melamine (Sigma-Aldrich, 99%) at 550 °C for 4 h in air. The as-synthesized In-TiO_2 and g-C_3N_4 were mixed at a weight ratio of 3:7 in 50 mL acetone in an ultrasound bath for 60 min. Finally, the mixture was stirred in a fume hood for 24 h to remove the acetone [25]. The as-obtained yellow solid powder was ground and calcined in a muffle furnace at 300 °C for 2 h.
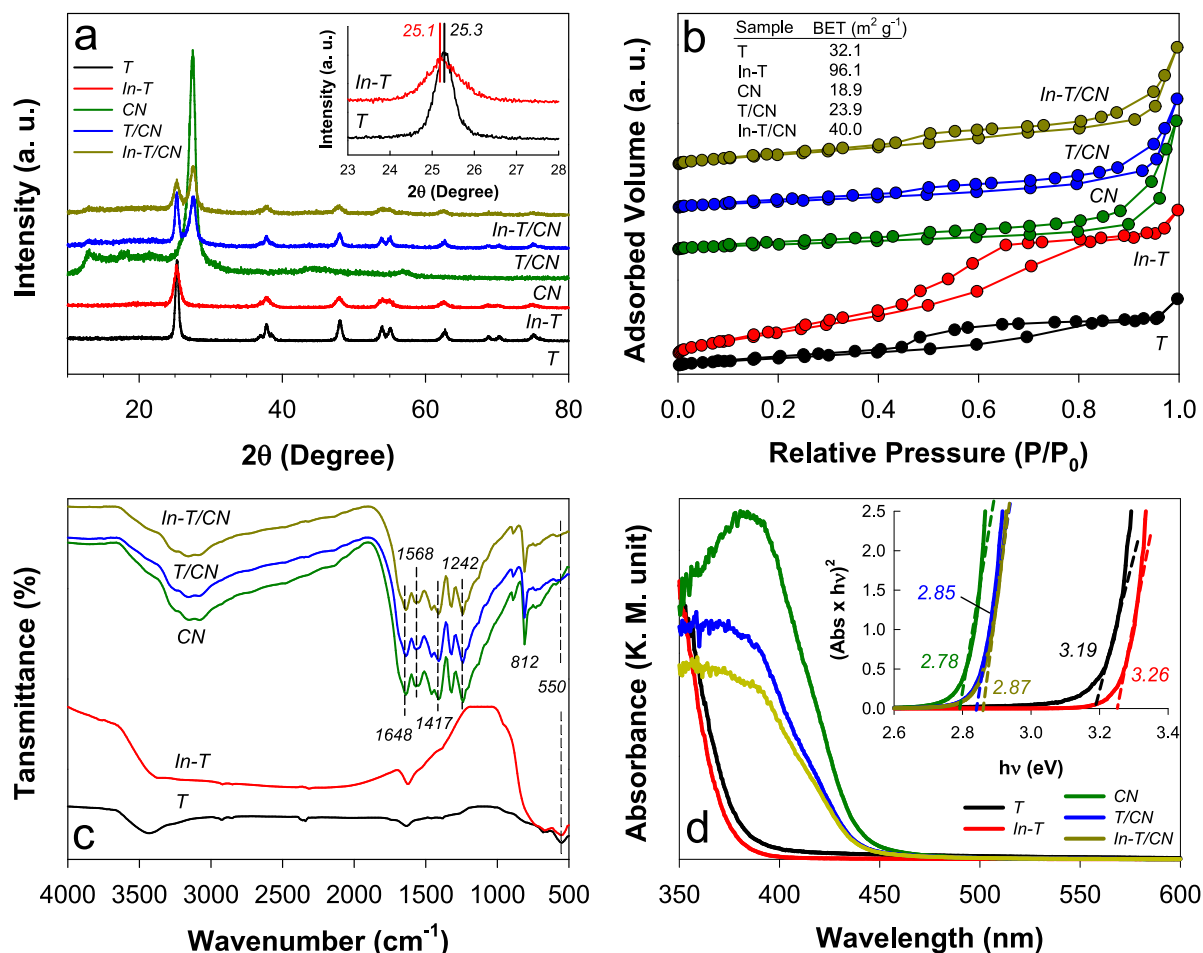
2.2. Surface characterizations

A low-temperature N_2 adsorption–desorption method (Quantachrome, Autosorb-iQ & Quadrasorb SI) was used to measure the BET surface area, pore-volume, and average pore diameter of the samples. High-resolution transmission electron microscopy (HR-TEM, FEI Company Titan G2) equipped with high-angle annular dark-field scanning TEM (HAADF-STEM) and energy-dispersive X-ray spectroscopy (EDS) was used to examine the morphology, lattice fringe, and elemental composition of the samples. The crystalline patterns and elemental states of the samples were examined using X-ray powder diffraction (XRD, Rigaku D/Max-2500) equipped with Cu Kα X-ray source ($\lambda = 1.5408$ Å) and X-ray photoelectron spectroscopy (XPS, ULVAC-PHI Quantera SXM) with Mg Kα monochromator X-ray source at 14 kV, respectively. The binding energies of the elements were calibrated with regards to C 1 s (284.8 eV). The diffuse reflectance UV–vis absorption spectra of the samples were obtained (Shimadzu, UV-2540). Sample powders were mixed with $BaSO_4$ and their reflectance spectra were measured with respect to $BaSO_4$. Then, the reflectance (R) was converted into absorbance using the Kubelka–Munk equation; absorbance = $(1 – R)^2/2R$. The Fourier transform infrared spectra (FTIR, PerkinElmer, Frontier) were collected in the wavenumber range of 400 cm^{-1} and 4000 cm^{-1} at a spectral resolution of 4 cm^{-1}. An inverted-type scanning confocal microscope (MicroTime-200, Picoquant, Germany) with a 40× (air) objective was used for the time-resolved photoluminescence lifetime (TRPL) study. Lifetime measurements were performed at the Korea Basic Science Institute, Daegu Center, Korea. Single-mode pulsed diode lasers ($\lambda = 375$ nm with a ~ 30 ps pulse width) were used as excitation sources. More information on the analytical conditions can be found elsewhere [12,26].

The adsorption–desorption isotherms of CO_2 gas on the as-synthesized photocatalysts were obtained using a BET analyzer (BELSORP-mini II, Japan Microtrac-BEL, Corp). Highly pure CO_2 gas (99.99%) at a pressure of 0–1 bar was adsorbed and desorbed at 298 K. The saturation vapor pressure was 1 bar when the relative pressure (p/p$_0$) was 1. The *in-situ* FTIR spectroscopic analysis was performed during photocatalytic reactions. The photocatalyst samples (50 mg) were placed in a 1×1 cm sample mount (RefractorReactor, Harrick). Before CO_2 adsorption, the samples were irradiated with simulated sunlight (100 mW cm^{-2}) for 1 h while purging high purity air to remove carbonaceous impurities adsorbed onto the samples. After the pre-phototreatment, no FTIR signals associated with carbonaceous chemicals were found. The reactor was purged with high-purity of CO_2 (99.99%) for 30 min and sealed. The FTIR spectra were obtained before and during the irradiation in the wavenumber range of 600–4000 cm^{-1} at a resolution of 4 cm^{-1} (Thermo Scientific). For each spectrum, 40 scans were automatically averaged. All spectra were referenced to the spectrum with the pre-phototreated surface before CO_2 adsorption.

2.3. Photoelectrochemical measurements and photocatalytic CO_2 reduction

The transient photocurrents of the as-synthesized sample electrodes were obtained in a customized glass reactor containing 0.5 M Na_2SO_4 aqueous solution using a three-electrode system with a saturated calomel electrode (SCE, reference electrode) and Pt wire (counter electrode). The sample electrodes were synthesized using a doctor blade method described elsewhere [27]. In brief, 5 mg of the sample powder was ultrasonicated in ethanol (10 mL) with a Nafion solution (5%, 20 μL, Sigma-Aldrich) and the sticky paste was coated on a fluorine-doped SnO_2-coated glass electrode. The sample electrodes were dried in air for 1 h and in an oven at 120 °C for 2 h. While a potential of + 0.5 V vs. SCE was applied to the sample electrodes, AM 1.5 light (100 mW cm^{-2}) was irradiated from a Xenon arc lamp (300 W).

Photocatalytic reactions were performed in a closed gas reactor using a UV LED generating $\lambda = 365$ nm (LUNA fiber optics) and visible light (λ

Fig. 1. Surface characterization of the as-synthesized TiO_2 (T), $In-TiO_2$ (In-T), $TiO_2/g-C_3N_4$ (T/CN), and $In-TiO_2/g-C_3N_4$ (In-T/CN) samples. (a) XRD spectra (inset: magnified spectra of TiO_2 and $In-TiO_2$). (b) N_2 adsorption–desorption isotherms (inset: BET surface areas). (c) FTIR spectra. (d) UV–vis absorption spectra (inset: optical analysis of bandgaps).

> 420 nm) of the simulated sunlight with an intensity of 100 mW cm^{-2} (300 W Xe lamp, ABET Technology). The wavelength intensity of the UV LED was estimated to be 0.9025 mW cm^{-2}, which was converted to an incident 365 nm-photon flux of $1.658 \times 10^{18} s^{-1}$. To use visible light, the simulated sunlight passed through a cutoff filter ($\lambda > 420$ nm, Newport). The catalyst powder (50 mg) was placed in the bottom of the stainless-steel reactor equipped with a quartz window for light penetration. Before photocatalysis, the samples were irradiated with light sources for 1 h while purging with high purity air to remove carbonaceous impurity adsorbed onto the samples. High-purity CO_2 (99.99%) or N_2 (99.999%) gases were then passed through a deionized water column and the reactor for 1 h. During irradiation (irradiated area: 1 cm^2), the head-space gases (i.e., CO, CH_4, and C_2H_4) were intermittently sampled and quantified using gas chromatography with a thermal conductivity detector (GC-TCD, Agilent 7820) and flame ionization detector (Young Lin ACME 6100 and Agilent 7820). To quantify CO and hydrocarbons, each standard gas (Fluka) was allowed to flow through the GC, and standard curve fits between each gas concentration and corresponding spectral area were obtained. Detailed analytical methods for CO and hydrocarbons have been described elsewhere [7,11,28]. After photocatalysis for 6 h, the photonic yield was estimated using the following equation: [2 × CO (mol) + 8 × CH_4 (mol) + 12 × C_2H_4 (mol)] × 100% / [photon flux × 6 h], where 2, 8, and 12 represent the equivalent numbers of electron for production of CO, CH_4, and C_2H_4, respectively, from CO_2.

3. Results and discussion

3.1. Surface characterization of the as-synesized materials

The XRD patterns of the as-synthesized samples (TiO_2, $In-TiO_2$, g-C_3N_4, $TiO_2/g-C_3N_4$, and $In-TiO_2/g-C_3N_4$) were compared (Fig. 1a). TiO_2 and $In-TiO_2$ showed an anatase crystalline structure (e.g., $2\theta = 25.3°$, $37.6°$, and $47.8°$ for (101), (004), and (200) planes, respectively; JCPDS no. 21–1272) [29]. The $In-TiO_2$ sample did not contain any indium-oriented peaks (e.g., In_2O_3) [30]. However, the (101) plane broadened and shifted to a low angle because of the In-oriented disorder of the TiO_2 lattice (Fig. 1a inset). The XRD pattern of g-C_3N_4 showed two characteristic peaks at $2\theta = 13.1°$ and $27.4°$, corresponding to (100) and (002) planes of g-C_3N_4, respectively (JCPDS no. 87–1526) [31]. The TiO_2 and g-C_3N_4 composite samples (i.e., $TiO_2/g-C_3N_4$ and $In-TiO_2/g-C_3N_4$) also showed the copresence of the crystal planes observed in the TiO_2 and g-C_3N_4. This indicates that g-C_3N_4 did not influence the TiO_2 structure during the synthetic processes of the composites. In line with this, the Raman spectroscopy of the composites did not show any new vibration modes (Fig. S1).

The N_2 adsorption–desorption isotherm measurement was used to evaluate pore distributions and specific surface areas of the as-synthesized samples (Fig. 1b). All samples showed mesoporous structures with hysteresis loops [32] and their textural properties were summarized in Table S2. Notably, In-doping increased the surface area of TiO_2 by three times (32 $m^2 g^{-1}$ to 96 $m^2 g^{-1}$) because of inhibited crystal growth. The as-synthesized, bulky g-C_3N_4 showed the lowest
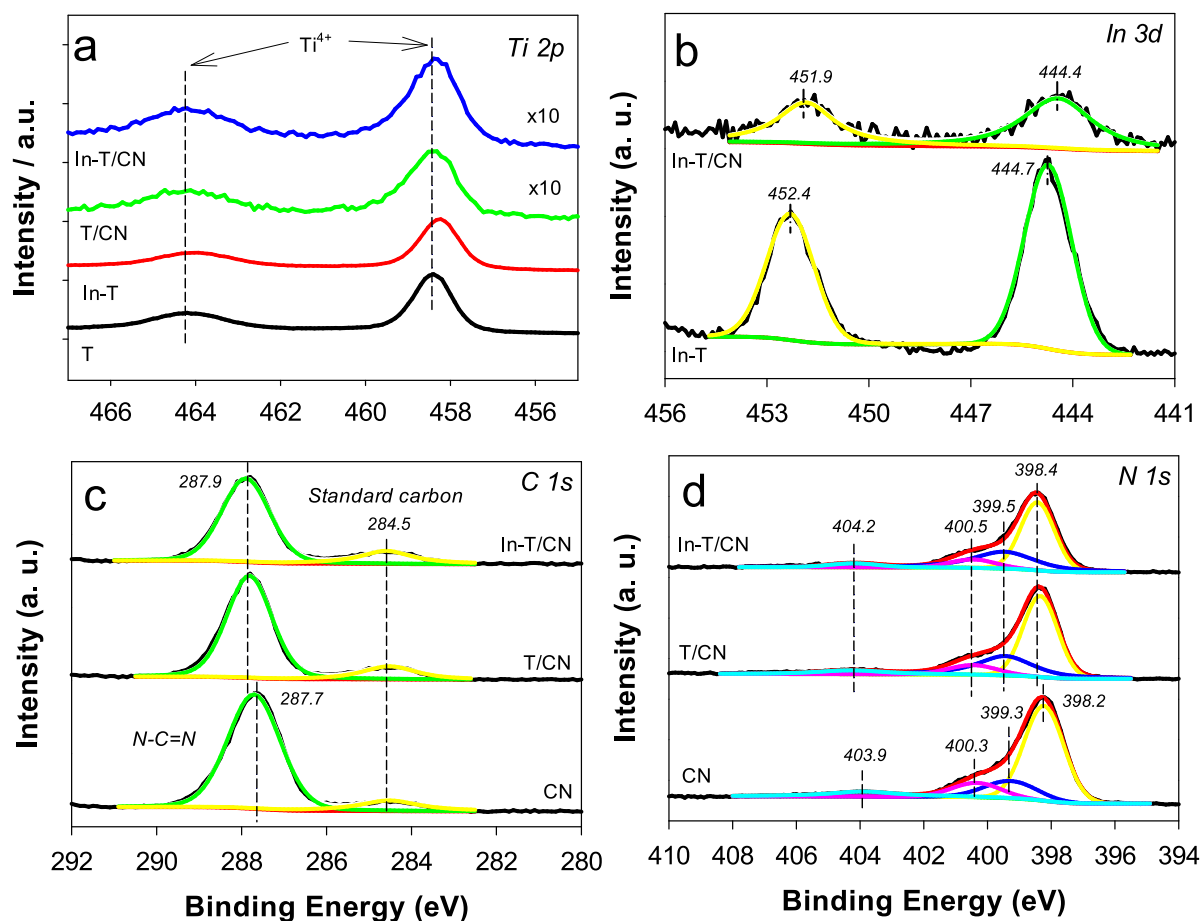
Fig. 2. XPS spectra of (a) Ti 2p, (b) In 3d, (c) C 1 s, and (d) N 1 s bands for In-TiO$_2$, g-C$_3$N$_4$, TiO$_2$/g-C$_3$N$_4$, and In-TiO$_2$/g-C$_3$N$_4$.

surface area of ~ 18 m^2 g^{-1}. When g-C$_3$N$_4$ was coupled with In-TiO$_2$, its surface area increased twofold.

The surface functional groups of the composites were also examined using FTIR (Fig. 1c). TiO$_2$ and In-TiO$_2$ samples showed broad absorption bands at ~ 3500 cm^{-1}, which were attributed to stretching vibrations of surface OH groups and adsorbed water molecules (H-O-H). The absorption at ~ 550 cm^{-1} was attributed to the Ti-O-Ti stretching vibration [33]. For g-C$_3$N$_4$, a broad absorption band at 3000–3600 cm^{-1} was associated with N–H stretching vibration of amino groups and/or O–H stretching of adsorbed water molecules [29]. Furthermore, many absorption peaks in the wavenumber region of 1200–1650 cm^{-1} were attributed to the typical stretching modes of g-C$_3$N$_4$. For example, the aromatic C-N stretching resulted in absorption peaks at 1242, 1417, and 1568 cm^{-1}. The peaks at 1648 and 812 cm^{-1} could be attributed to the C-N stretching and characteristic breathing mode of triazine units, respectively [34]. All these characteristic bands of TiO$_2$ and g-C$_3$N$_4$ were found in the composite samples, indicating that the chemical structures of both components remained intact during the synthetic processes of the composites.

The UV–vis reflectance absorption spectra of the as-synthesized samples were obtained to estimate the optical E$_g$ values (Fig. 1d and S2). Compared to bare TiO$_2$, In-TiO$_2$ exhibited a slightly blue-shifted absorption spectrum without any new absorption band. However, g-C$_3$N$_4$ showed an absorption peak at ~ 400 nm and an edge at ~ 450 nm. The spectrum of TiO$_2$/g-C$_3$N$_4$ was similar to that of g-C$_3$N$_4$, but with a slight blue shift in the absorption edge. In-TiO$_2$/g-C$_3$N$_4$ followed the same tendency as TiO$_2$/g-C$_3$N$_4$, with the reduced absorbance attributed to the In-doping effect [18]. Based on these spectra, the optical E$_g$ values were estimated to be 3.19 eV (TiO$_2$), 3.26 eV (In-TiO$_2$), 2.78 eV (g-C$_3$N$_4$), 2.85 eV (TiO$_2$/g-C$_3$N$_4$), and 2.87 eV (In-TiO$_2$/g-C$_3$N$_4$) (Fig. 1d

inset). The increase in E$_g$ caused by In-doping was partly attributed to In$_2$O$_3$ with a large E$_g$ (3.7 eV) [18]. In some cases, absorption in the visible region of 400–800 nm was observed with In-TiO$_2$ synthesized with an indium chloride precursor [35] because of the surface states of O-In-Cl$_x$ species. However, in this study, a different precursor (indium nitrate) was used and no visible light absorption with In-TiO$_2$ alone was observed.

The elemental states of the as-synthesized samples were examined using XPS analysis (Fig. 2 and S3). The bare TiO$_2$ spectrum showed Ti 2p bands at ~ 458.4 eV (2p3/2) and ~ 464. 2 eV (2p1/2) associated with Ti^{4+} states (Fig. 2a). In-TiO$_2$ showed the same Ti 2p bands, at 0.2 eV-lower binding energies [36]. This sample also contained two In 3d-bands at ~ 452.4 (3d3/2) and ~ 444.7 (3d5/2) (Fig. 2b), which were attributed to In^{3+} species [35,37]. It appears that In^{3+}-doping of the TiO$_2$ lattice partially reduced Ti^{4+} to Ti^{3+}, creating oxygen vacancies favorable for CO$_2$ adsorption [38–40]. Notably, the coupling of In-TiO$_2$ (or TiO$_2$) and g-C$_3$N$_4$ significantly influenced the binding energies of the elements in both materials. For example, the binding energy of the In 3d-bands decreased by ~ 0.4 eV (Fig. 2b) and the C 1 s band in the bare g-C$_3$N$_4$ was shifted to high binding energy by 0.2 eV. However, the binding energy of standard carbon was unchanged (Fig. 2c). Considering that the binding energy of C 1 s band in g-C$_3$N$_4$ is susceptible to electronegativity of neighboring elements [29,41], such shift indicates a strong interaction between In-TiO$_2$ and g-C$_3$N$_4$. The bare g-C$_3$N$_4$ also demonstrated N 1 s bands originating from C $-$ N $=$ C, N$-$(C)$_3$, C $-$ N $-$ H, and π-excitation at binding energies of 398.6, 399.4, 400.9, and 404.2 eV, respectively (Fig. 2d) [42–44]. The sub-N 1 s bands were also shifted to high binding energy by 0.2 eV. Accordingly, these shifts in the binding energies of the component elements indicate strong electronic interaction between In-TiO$_2$ (or TiO$_2$) and g-C$_3$N$_4$.
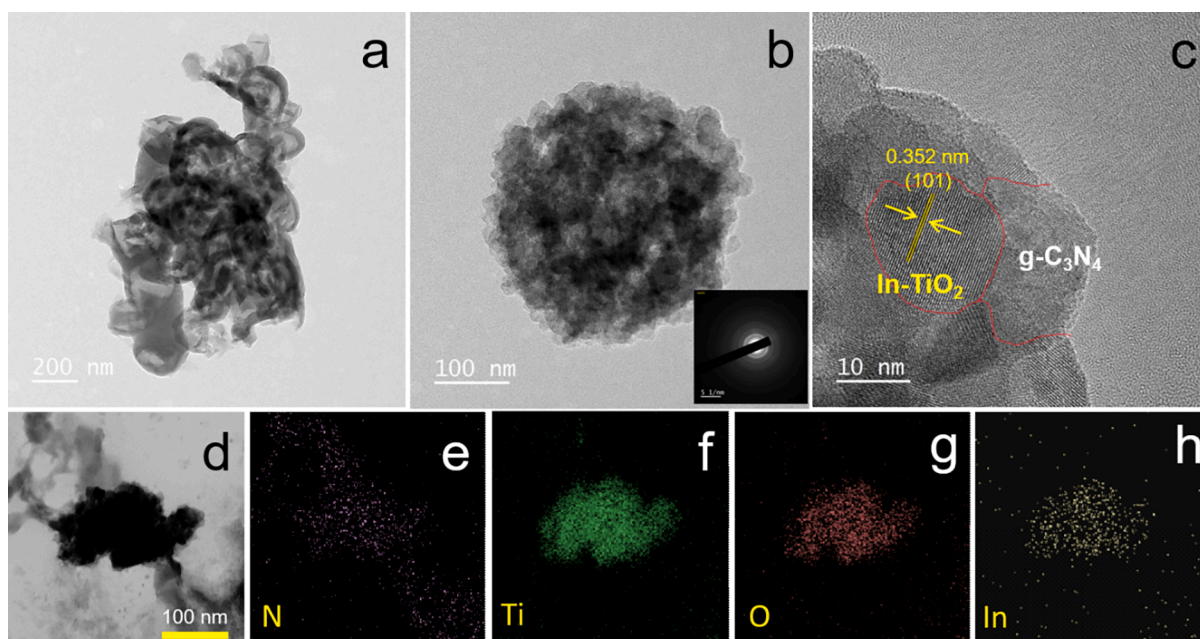
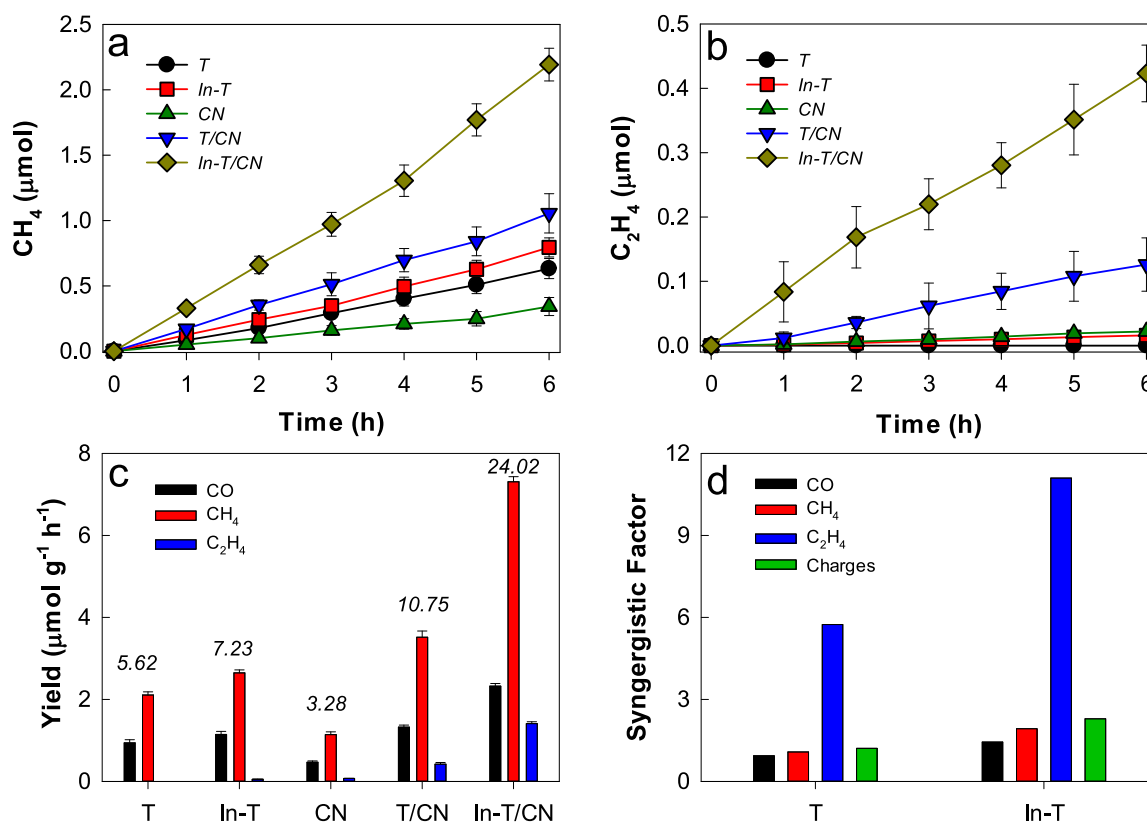**Fig. 3.** (a and b) TEM, (c) HR-TEM, (d) HAADF-STEM image, and (e-h) EDS elemental mappings of In-TiO$_2$/g-C$_3$N$_4$.

Fig. 4. Photocatalytic CO$_2$ conversions with the as-synthesized TiO$_2$, In-TiO$_2$, TiO$_2$/g-C$_3$N$_4$, and In-TiO$_2$/g-C$_3$N$_4$ samples under UV irradiation. (a) CH$_4$ productions. (b) C$_2$H$_4$ productions. (c) Comparison of product yields after 6 h. The numbers on the bars stand for the total elementary charges (μmol) used for the products (2e$^-$, 8e$^-$, and 12e$^-$ for CO, CH$_4$, and C$_2$H$_4$, respectively). (d) Synergistic factors of TiO$_2$ and In-TiO$_2$ activities by g-C$_3$N$_4$ for CO$_2$ conversion products and elementary charges. Synergistic factor = activity of TiO$_2$/g-C$_3$N$_4$ (or In-TiO$_2$/g-C$_3$N$_4$) divided by the sum of TiO$_2$ (or In-TiO$_2$) activity and g-C$_3$N$_4$ activity.

The morphology of In-TiO$_2$/g-C$_3$N$_4$ composites was examined using TEM and HR-TEM (Fig. 3). The various morphologies of the same sample were attributed to the impregnation method which often results in irregular configuration. The lattice plane of anatase (1 0 1) with a lattice spacing of 0.325 nm was observed, indicating In-TiO$_2$ inside the composites. While forming interfacial contact with In-TiO$_2$, ~ 10 nm-thick g-C$_3$N$_4$ was located on the edge of the composite. EDS mapping of the In-TiO$_2$/g-C$_3$N$_4$ composites showed that In and Ti were uniformly
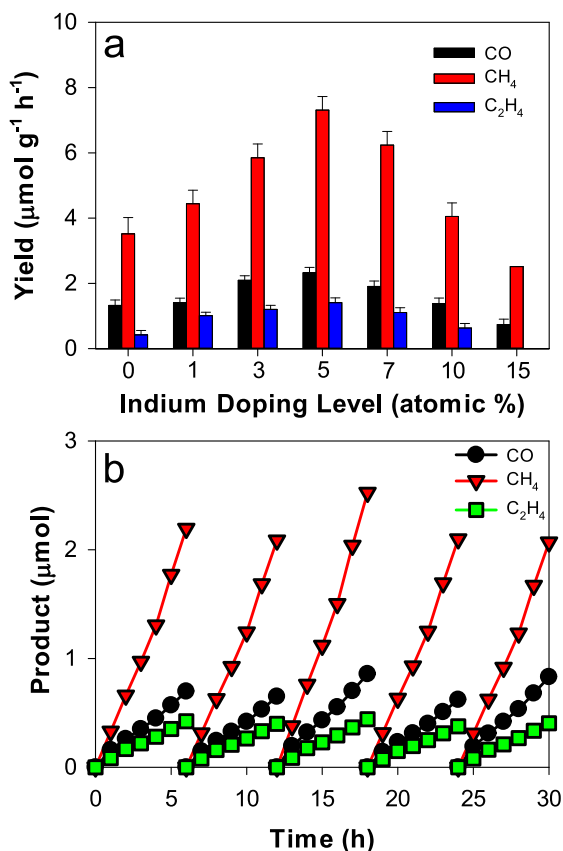
Fig. 5. Photocatalytic CO_2 conversions with the as-synthesized In-TiO₂/g-C₃N₄ samples under UV irradiation. (a) Effect of In-doping level. (b) Prolonged photocatalysis.

distributed in the same region. N atoms also were found in the In and Ti regions (**Fig. S4**) and further spread from the regions. This indicates that g-C₃N₄ acts as a linker of In-TiO₂ particles while forming a composite.

3.2. Photocatalytic CO₂ conversion under UV and visible light

The photocatalytic CO_2 conversion was conducted using the as-synthesized samples under UV (λ = 365 nm) (Fig. 4). The primary CO_2 conversion products were CO, methane, and ethylene, which were linearly produced with time (see **Fig. S5** for CO production). The yield was 2–3 times greater than the CO yield for all samples. Trace levels of ethylene were produced on irradiated TiO₂, In-TiO₂, and g-C₃N₄, whereas the amount of ethylene was comparable to CO with In-TiO₂/g-C₃N₄. When the reactor was filled with N₂ instead of CO_2, no carbonaceous compound was detected (**Fig. S6**). This implies that the purged CO_2 was the sole carbon source of the compounds.

The photocatalytic activity of bare and modified samples was also compared. TiO₂ and g-C₃N₄ showed poor activity, whereas TiO₂/g-C₃N₄ showed significant photocatalytic activity (Fig. 4**a and 4b**). For example, TiO₂/g-C₃N₄ produced 1.7 times and 3 times more methane than those with TiO₂ and g-C₃N₄, respectively. A similar enhancement was similarly found for CO (**Fig. S5**). In-TiO₂/g-C₃N₄ demonstrated a more pronounced coupling effect. The amount of methane with In-TiO₂/g-C₃N₄ was ~ 2.8 times and 6.4 times larger than those with In-TiO₂ and g-C₃N₄, respectively (Table S3). Notably, ethylene production with In-TiO₂/g-C₃N₄ was 26.5 times and ~ 19 times larger than that with In-TiO₂ and g-C₃N₄, respectively. The synergistic factors [i.e., the activity of In-TiO₂/g-C₃N₄ (or TiO₂/g-C₃N₄) divided by the sum of In-TiO₂ (or TiO₂) activity and g-C₃N₄ activity] were estimated for CO, methane, and ethylene (Fig. 4**c**). The synergistic factors for CO, methane, and ethylene by g-C₃N₄ with TiO₂, were 0.9, 1.1, and 5.7, respectively; with In-TiO₂,

they were 1.4, 1.9, and 11, respectively. This shows that the coupling effect of g-C₃N₄ became more significant as more reduced chemicals were produced ($12e^-$, $8e^-$, and $2e^-$-transfers for ethylene, methane, and CO, respectively). Notably, the fractional ratios of CO, methane, and ethylene were ~ 29%, 68%, and < 4%, respectively, with each In-TiO₂ and g-C₃N₄, whereas with In-TiO₂/g-C₃N₄, they changed to 21%, 66%, and 13%, respectively. This indicates that In-doping facilitated the charge transfer kinetics in increasing the ethylene selectivity. The total number of photogenerated charges used for CO_2 conversion (for 6 h) was ~ 10.8 μmole with TiO₂/g-C₃N₄ and 24.0 μmole with In-TiO₂/g-C₃N₄ (Fig. 4**c**), leading to the synergistic factors of ~ 1.2 and 2.3, respectively (Fig. 4**d**). The overall photonic yield with In-TiO₂/g-C₃N₄ was 40.4% (2.4% for CO, 29.5% for methane, and 8.5% for ethylene) (Table S3).

The as-observed activity of In-TiO₂/g-C₃N₄ significantly depended on the In-doping level (Fig. 5**a**). The yield products of CO, methane, and ethylene were greatest with the In-doping of 5 atomic%. The existence of the optimal doping level indicates that In played a critical role in the photogenerated charge transfer kinetics (discussed below). CO was always observed regardless of the In-doping level, whereas neither H₂ nor other carbonaceous compounds (e.g., formate) were detected in all cases. The proton-coupled electron (H^+/e^- or $H^\bullet$) transfer (PCET) appeared to be the predominant pathway of methane and ethylene production and the direct CO_2 reduction by photogenerated electrons did not occur (Scheme 1). A prolonged photocatalysis over 30 h with the as-synthesized In-TiO₂/g-C₃N₄ showed continuous production of carbonaceous compounds with no sign of material deactivation (Fig. 5**b**). This stability with high activity is impressive because materials with high activities usually suffer from rapid deactivation whereas those with low activities exhibit relatively prolonged stability [6,11–13]. It appears that an efficient charge transfer between In-TiO₂ and g-C₃N₄ effectively inhibits the photo-induced deactivation (e.g., photocorrosion) of each component.

The photocatalytic activity of the as-synthesized samples was also examined under visible light (λ > 420 nm) (Fig. 6). Any CO_2 conversion product was not observed with TiO₂ and In-TiO₂ under visible light (Fig. 6**a and 6b**), because of their E_g of ~ 3.2 eV. However, g-C₃N₄ with E_g of 2.78 eV generated photo charges and produced CO and CH₄ at the ratio of ~ 3:7. Therefore, g-C₃N₄ was essential for driving the CO_2 reduction reaction under visible light. The overall tendency of the activity was similar to that under UV. In-doping and g-C₃N₄-coupling enhanced TiO₂ activity, leading to the highest activity with In-TiO₂/g-C₃N₄ (Fig. 6**c**). The optimal In-doping level was the same as that observed under UV (**Fig. S7**). However, CO was the most abundant with ~ 60% selectivity, whereas ethylene was not produced. The synergistic factors with TiO₂/g-C₃N₄ for the CO and methane production were 9 and 2, respectively; the values with In-TiO₂/g-C₃N₄ were 21 and 5, respectively (Fig. 6**d**). The total number of photogenerated charges used for CO_2 conversion (for 6 h) was 7.8 μmole with TiO₂/g-C₃N₄ and 20 μmole with In-TiO₂/g-C₃N₄ (Fig. 6**c**), resulting in synergistic factors of 2.6 and 6.7, respectively (Fig. 6**d**).

3.3. Photoinduced charge transfer and photocatalytic CO₂ conversion mechanism

To examine the In-doping and g-C₃N₄-coupling effects on the photoinduced behavior, the PL emission spectra of the as-synthesized samples were compared (Fig. 7**a**). Upon excitation at λ = 375 nm, all the samples exhibited the similar spectral responses with broad emission bands in the wavelength range from 400 to 700 nm. The main emission band with bare TiO₂ was found at λ = ~630 nm because of the recombination of trapped electrons and holes [45,46]. The emission band was shifted to λ ~ 560 nm and its intensity was reduced because of the In 5 s state [17]. In contrast to these TiO₂-based PL spectra, the g-C₃N₄ generated a significant emission at λ ~ 470 nm. Notably, this band was significantly reduced when coupled to In-TiO₂, indicating that the
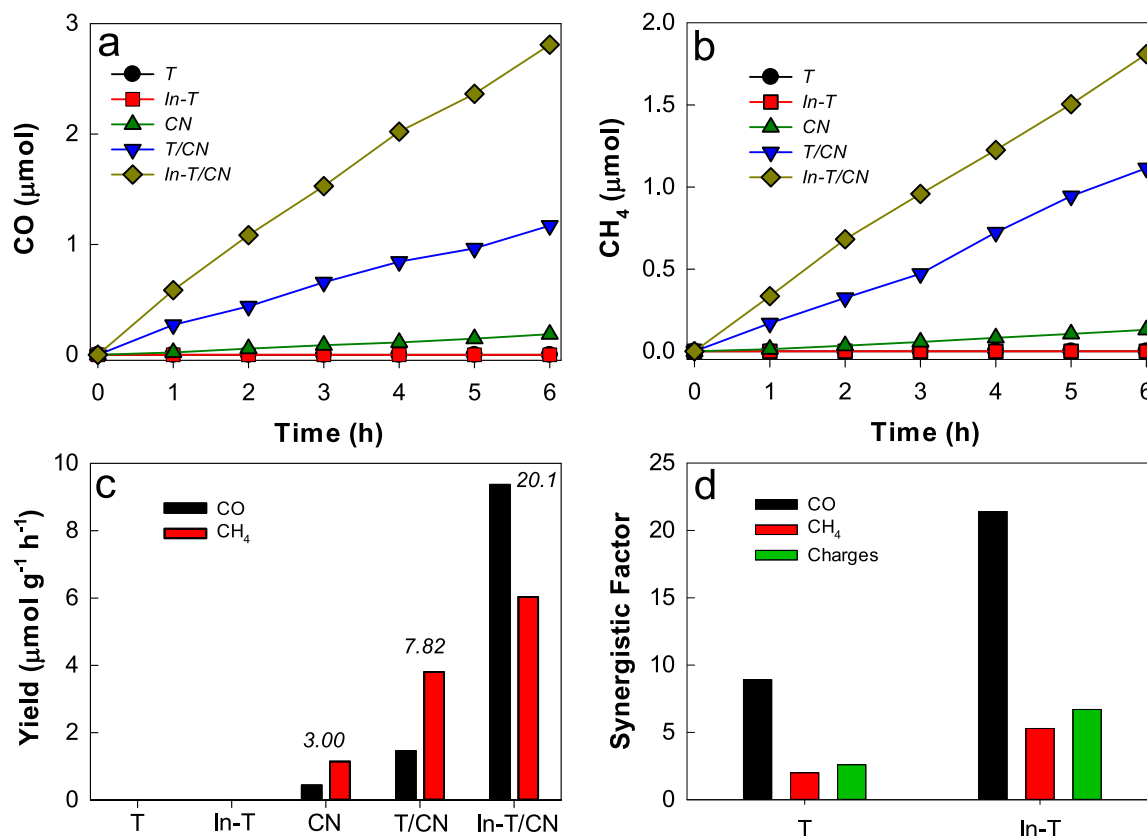
Fig. 6. Photocatalytic CO_2 conversions with the as-synthesized TiO_2, In-TiO_2, TiO_2/g-C_3N_4, and In-TiO_2/g-C_3N_4 samples under visible light. (a) CO productions. (b) CH_4 productions. (c) Comparison of product yields after 6 h. The numbers on the bars stand for the total elementary charges (μmol) used for the products ($2e^-$, $8e^-$, and $12e^-$ for CO, CH_4, and C_2H_4, respectively). (d) Synergistic factors of TiO_2 and In-TiO_2 activities by g-C_3N_4 for CO_2 conversion products and elementary charges.

charge recombination was inhibited in In-TiO_2/g-C_3N_4 [29,47].

TRPL decay spectra of the samples excited at λ = 375 nm were compared (Fig. 7b) to gain insights into the charge transfer kinetics. The PL intensity of TiO_2 decayed rapidly with an average decay lifetime (τ) of 3.19 ns, whereas In-TiO_2 showed a twofold slower τ (7.4 ns). This confirms that charge carriers survived for longer periods and their recombination is retarded with In-TiO_2. Notably, τ with g-C_3N_4 increased from 5.8 ns to 6.73 ns and 18 ns when g-C_3N_4 was coupled with TiO_2 and In-TiO_2, respectively. The slowest PL decay with In-TiO_2/ g-C_3N_4 was attributed to the synergetic effect of In-associated trap sites and delocalized π-electrons over the molecular framework in g-C_3N_4 [48]. This should inhibit the recombination of photogenerated charge carriers by facilitating the interfacial charge transfer, allowing the charge carriers to survive long enough for reaction with adsorbed CO_2. The 2D PL images of the as-synthesized samples further revealed that the charge carrier transfer kinetics were relatively uniform over the composite samples (Fig. 7b inset). The strong junction between In-TiO_2 and g-C_3N_4 appears to effectively separate electrons and holes, resulting in a low PL emission.

A comparison of photocurrent density (J_{ph}) verified the inhibited charge recombination with In-TiO_2/g-C_3N_4 (Fig. 7c). Bare TiO_2 generated small J_{ph} of < 2 μA cm^{-2}, and In-doping slightly enhanced J_{ph}. g-C_3N_4 showed a lower activity than TiO_2 and In-TiO_2; however, J_{ph} with g-C_3N_4 was stable over time. J_{ph} with In-TiO_2/g-C_3N_4 was 5 μA cm^{-2}, which was greater than each In-TiO_2 and g-C_3N_4, as well as the sum of both. Furthermore, it was maintained over time without a sign of decrease. TiO_2/g-C_3N_4 showed the same tendency.

The CO_2 adsorption isotherms were also obtained to examine the CO_2 adsorption capacities of the as-synthesized photocatalysts (Fig. 8). All adsorption–desorption isotherms were found to be reversible without hysteresis (Fig. S8), indicating that CO_2 is physically adsorbed

without forming chemical bonds. The CO_2 adsorbed on bare TiO_2 was estimated to be 0.13 mmol g^{-1}, whereas In-doping enhanced CO_2 adsorption capacity by nearly twofold (0.25 mmol g^{-1}). This In-doping effect was similarly found in the BET surface area, which was ~ 3-fold enhanced upon In-doping (Fig. 1b). Note that the CO_2 adsorption capacity of g-C_3N_4 (~0.08 mmol g^{-1}) was only 25% that of In-TiO_2. In-TiO_2/g-C_3N_4, with a weight ratio of 3/7 had a lower capacity than that for In-TiO_2 without g-C_3N_4 (the same for TiO_2). Therefore, In-TiO_2 should act as a CO_2 adsorbent and photocatalyst, whereas g-C_3N_4 mainly acts as a photocatalyst in the CO_2 RR with the In-TiO_2/g-C_3N_4 composites. The tendency for the CO_2 adsorption capacity was similar to that for the BET area (Fig. 8 inset).

To gain insight into the reaction mechanism, in-situ FTIR spectra of In-TiO_2/g-C_3N_4 during photocatalysis under UV and visible light were obtained (Fig. 9). The surface without CO_2 adsorption was clean with no specific absorption signals. However, the surface exposed to CO_2 gas exhibited many absorption signals at wavenumbers of 944–1076 cm^{-1} ($CO_2 \cdot H_2O$, HCO_3^-, and CO_3^{2-}), 2345 cm^{-1} (CO_2), and 3625 cm^{-1} (HCO_3^- or CO_2) [49,50]. With UV irradiation, two absorption bands appeared at 2985 cm^{-1} and 3155 cm^{-1} corresponding to C–H stretching vibrations of CH_4 and C_2H_4, respectively (Fig. 9a). The wavenumber of 1295 cm^{-1} was also attributed to the C–H stretching vibration of CH_4. The surface irradiated with visible light showed similar spectral patterns, except for the absence of absorbance at 3155 cm^{-1} (C_2H_4) (Fig. 9b). This is consistent with the gaseous products obtained under UV (CO, CH_4, and C_2H_4) and visible light (CO and CH_4). The absence of CO stretching mode in the wavenumber range of 2100–2200 cm^{-1} was attributed to the limited adsorption of CO on In-TiO_2/g-C_3N_4 (Fig. S9).

All observed results indicate that In-TiO_2/g-C_3N_4 is active for photoinduced charge transfer and photocatalytic CO_2 conversion under UV and visible light. Under UV, In-TiO_2 and g-C_3N_4 are both activated;
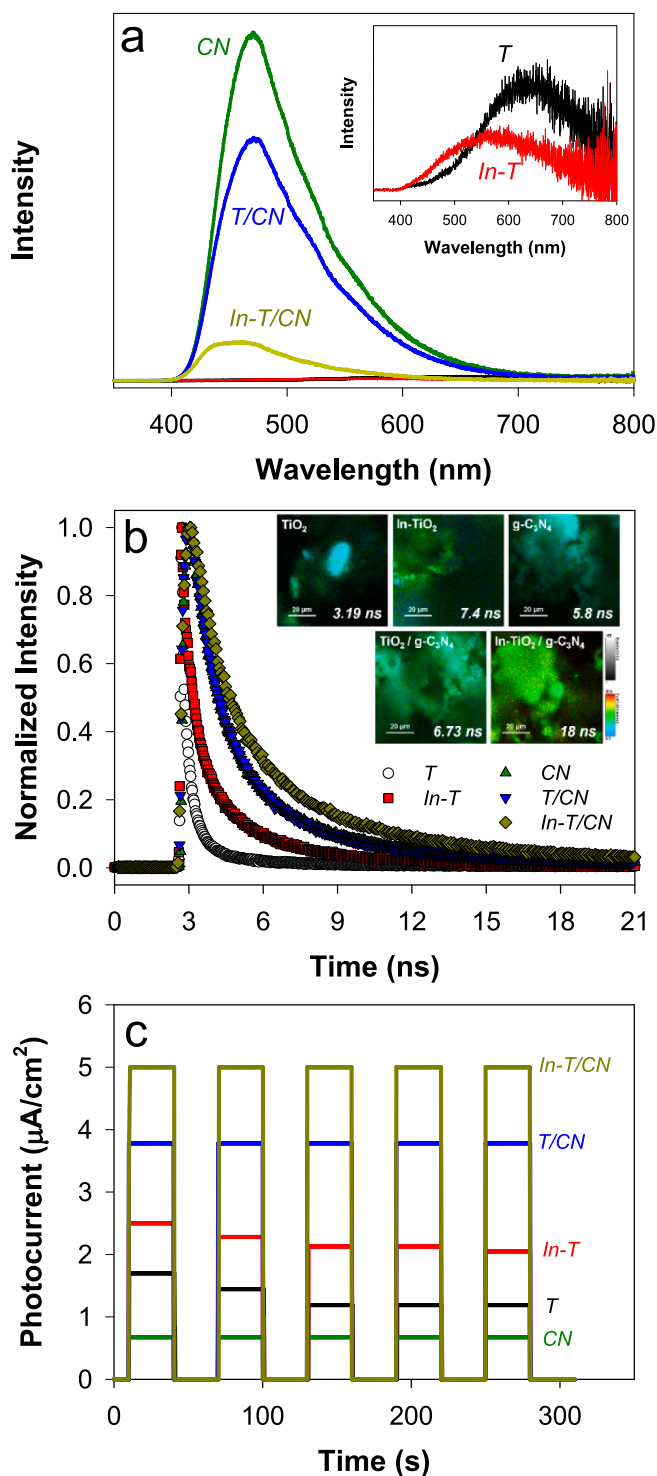
Fig. 7. Spectroscopic and photoelectrochemical analysis of the as-synthesized samples. (a) Photoluminescence spectra excited at λ = 375 nm. The inset shows the magnified spectra of TiO_2 and $In-TiO_2$. (b) Time-resolved photoluminescence emission decay spectra. Excited at λ = 375 nm. The inset shows the two-dimensional emission intensity and lifetime images. The numbers in the images represent the average lifetimes (τ). (c) Chopped photocurrent profiles at E = 0.5 V vs. SCE in 0.5 M sodium sulfate solutions.

Fig. 8. CO_2 adsorption isotherms with the as-synthesized samples at 298 K. The numbers in parentheses represent the amounts of adsorbed CO_2 at 1 atm CO_2 gas (mmol g^{-1}). Inset shows the plot between the BET surface areas and the amounts of adsorbed CO_2 for the same samples.
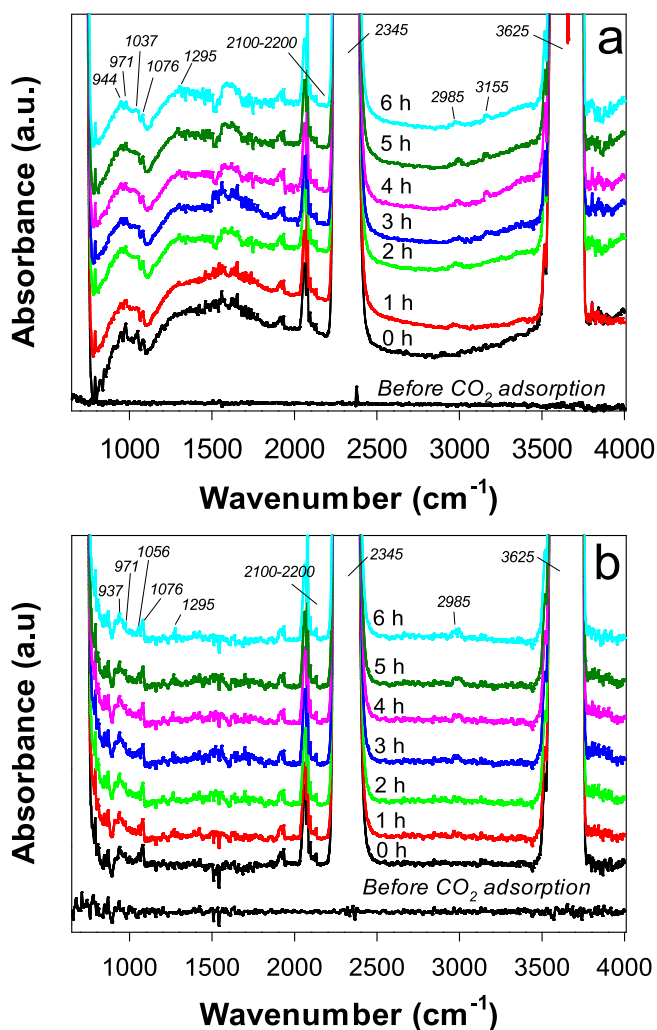
Fig. 9. In-situ FTIR spectra of $In-TiO_2/g-C_3N_4$ surface in the CO_2 atmosphere under (a) UV and (b) visible light.

under visible light, only g-C_3N_4 is activated (Scheme 1). The different band energy levels of the two semiconductors can induce cascaded charge transfer under UV [51]. Therefore, regardless of the irradiation condition, the photogenerated electrons in g-C_3N_4 are transferred to In-TiO_2 with high CO_2 adsorption capacity and the photogenerated hole-

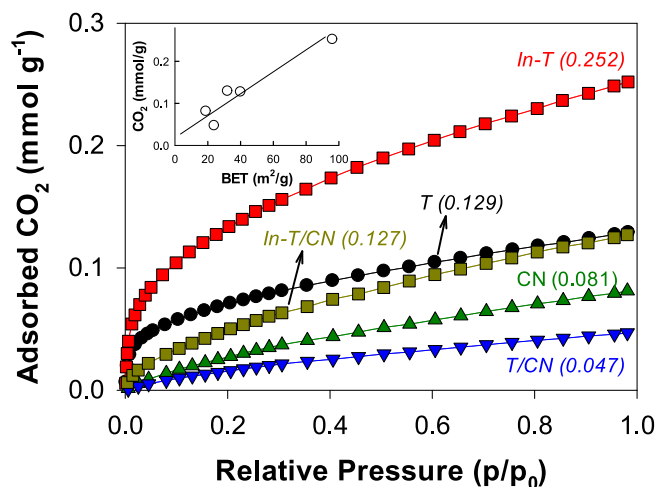reaction occurs on g-C$_3$N$_4$ with low CO$_2$ adsorption capacity. The high J_{ph} and long τ with In-TiO$_2$/g-C$_3$N$_4$ (*see* Fig. 7) indicate that the charge separation occurs efficiently, and the separated charge carriers sufficiently survive for transfer to adsorbed CO$_2$ (*CO$_2$). According to density functional theory computations, the CO$_2$ adsorption energy on TiO$_2$ surface is strongly influenced by crystalline structures and oxygen vacancies [38,52,53]. For the anatase (1 0 1) surface, the monodentate binding modes (e.g., O-C-O – Ti$_{surf}$ and O-C – O$_{surf}$) have the exothermic adsorption energies between -7.8 and -11 kcal mol^{-1}, whereas the adsorption energy for the bidentate modes significantly decreases. Notably, the presence of oxygen vacancies largely enhances the CO$_2$ adsorption energies for both binding modes. For example, the adsorption energy of CO$_2$ via the monodentate mode for the anatase TiO$_2$ (1 0 1) with oxygen vacancies (-15.5 kcal mol^{-1}) is greater than the adsorption energy of CO$_2$ with g-C$_3$N$_4$ (-9.64 kcal mol^{-1}) [38,40,54]. Considering that In-doping induced Ti^{3+} species with oxygen vacancies (see Fig. 2a), In-TiO$_2$ should be better than g-C$_3$N$_4$ for CO$_2$ adsorption.

The CO production under UV and visible light also indicates that the photogenerated electrons are transferred to a carbon atom of *CO$_2$ in the initial stage [19,32,55]. If an oxygen atom of *CO$_2$ is an electron acceptor, the aliphatic acids should have been produced instead [6,11,13,56]. In-TiO$_2$ has a lower CB than the one-electron reduction potential of free CO$_2$ [$E°(CO_2/CO_2^{\bullet-}) = -1.97$ V] [57]. Accordingly, PCET (not electron transfer) should be the primary pathway for *CO$_2$ reduction. Despite similar thermochemical potentials for H$_2$ and CO production [$E°(H_2O/H_2) = 0$ V; $E°(CO_2/CO) = -0.106$ V], the absence of H$_2$ production indicates that the dimerization of two H$^\bullet$s did not occur and that the reaction between H$^\bullet$ and CO$_2$ was dominant (Scheme 1c). The produced CO should undergo stepwise PCET, forming methane and ethylene. Such photocatalyzed Fischer-Tropsch reaction was also observed in previous studies [7,28]. Finally, the photogenerated holes were speculated to oxidize adsorbed water to surface-bound OH radicals ($>$OH$^\bullet$) and H$^+$. The dimerization of the two radical species can form hydrogen peroxide, which can be actively involved in photochemical and photocatalytic reactions. The absence of O$_2$ in the reactor headspace supports this speculation.

4. Conclusions

This study demonstrated that In-TiO$_2$/g-C$_3$N$_4$ composites synthesized using a facile impregnation method converted CO$_2$ into value-added chemicals with high efficiency under UV and visible light. The primary CO$_2$ conversion products were CO, methane, and ethylene under UV, and CO and methane under visible light. A prolonged photocatalysis with In-TiO$_2$/g-C$_3$N$_4$ produced the same carbonaceous compounds for 30 h, with a photonic yield of $\sim$ 40% (2.4% for CO, 29.5% for methane, and 8.5% for ethylene). The enhanced UV and visible light activities were attributed to synergistic effects of doping with In and coupling with g-C$_3$N$_4$. While In-doping facilitated charge transfer via In^{3+}-associated trap sites, a strongly coupled g-C$_3$N$_4$ induced cascaded charge transfer. The photoelectrochemical response and time-resolved photoluminescence spectra confirmed the significantly inhibited charge recombination and prolonged charge carriers, particularly with In-TiO$_2$/g-C$_3$N$_4$. The CO$_2$ adsorption isotherms indicated that In-TiO$_2$ acts as a primary CO$_2$ adsorbent and photocatalyst, whereas g-C$_3$N$_4$ mainly acts as a photocatalyst. In-situ FTIR study further revealed the formation of CH$_4$ and C$_2$H$_4$ under UV and CH$_4$ under visible light on In-TiO$_2$/g-C$_3$N$_4$. Considering that In-TiO$_2$ surface is the same CO$_2$ reduction site under UV and visible light, the absence of ethylene production under visible light was attributed to insufficient PECT in the last stage of the stepwise CO$_2$ reduction (CO$_2$ → CO → CH$_4$ → C$_2$H$_4$).

Declaration of Competing Interest

The authors declare that they have no known competing financial interests or personal relationships that could have appeared to influence the work reported in this paper.

Appendix A. Supplementary data

Supplementary data to this article can be found online at https://doi.org/10.1016/j.cej.2022.135388.

References

[1] M. Halmann, Photoelectrochemical reductoin of aqueous carbon dioxide on p-GaP in liquid junction solar cells, Nature 275 (1978) 115–116, https://doi.org/10.1038/275115a0.

[2] T. Inoue, A. Fujishima, S. Konishi, K. Honda, Photoelectrocatalytic reduction of carbon dioxide in aqueous suspensions of semiconductor powders, Nature 277 (5698) (1979) 637–638, https://doi.org/10.1038/277637a0.

[3] J.-M. Lehn, R. Ziessel, Photochemical generation of carbon monoxide and hydrogen by reduction of carbon dioxide and water under visible light irradiation, Proc. Natl. Acad. Sci. U.S.A. 79 (2) (1982) 701–704, https://doi.org/10.1073/pnas.79.2.701.

[4] B.A. Parkinson, P.F. Weaver, Photoelectrochemical pumping of enzymatic CO$_2$ reduction, Nature 309 (5964) (1984) 148–149, https://doi.org/10.1038/309148a0.

[5] M.R. Hoffmann, J.A. Moss, M.M. Baum, Artificial photosynthesis: Semiconductor photocatalytic fixation of CO$_2$ to afford higher organic compounds, Dalton Trans. 40 (2011) 5151–5158, https://doi.org/10.1039/C0DT01777A.

[6] S.Y. Choi, S.H. Yoon, U. Kang, D.S. Han, H. Park, Standalone photoconversion of CO$_2$ using Ti and TiO$_x$-sandwiched heterojunction photocatalyst of CuO and CuFeO$_2$ films, Appl. Catal. B 288 (2021) 119985, https://doi.org/10.1016/j.apcatb.2021.119985.

[7] H. Park, H.-H. Ou, A.J. Colussi, M.R. Hoffmann, Artificial photosynthesis of C1–C3 hydrocarbons from water and CO$_2$ on titanate nanotubes decorated with nanoparticle elemental copper and CdS quantum dots, J. Phys. Chem. A 119 (19) (2015) 4658–4666, https://doi.org/10.1021/jp511329d.

[8] C. Bie, B. Zhu, F. Xu, L. Zhang, J. Yu, In situ grown monolayer N-doped graphene on CdS hollow spheres with seamless contact for photocatalytic CO$_2$ reduction, Adv. Mater. 31 (42) (2019) 1902868, https://doi.org/10.1002/adma.201902868.

[9] Z.-C. Kong, J.-F. Liao, Y.-J. Dong, Y.-F. Xu, H.-Y. Chen, D.-B. Kuang, C.-Y. Su, Core@shell CsPbBr$_3$@zeolitic imidazolate framework nanocomposite for efficient photocatalytic CO$_2$ reduction, ACS Energy Lett. 3 (11) (2018) 2656–2662, https://doi.org/10.1021/acsenergylett.8b01658.

[10] S. Sorcar, J. Thompson, Y. Hwang, Y.H. Park, T. Majima, C.A. Grimes, J.R. Durrant, S.-I. In, High-rate solar-light photoconversion of CO$_2$ to fuel: Controllable transformation from C1 to C2 products, Energy Environ. Sci. 11 (11) (2018) 3183–3193, https://doi.org/10.1039/C8EE00983J.

[11] U. Kang, S.H. Yoon, D.S. Han, H. Park, Synthesis of aliphatic acids from CO$_2$ and water at efficiencies close to the photosynthesis limit using mixed copper and iron oxide films, ACS Energy Lett. 4 (9) (2019) 2075–2080, https://doi.org/10.1021/acsenergylett.9b01281.

[12] U. Kang, H. Park, A facile synthesis of CuFeO$_2$ and CuO composite photocatalyst films for production of liquid formate from CO$_2$ and water over a month, J. Mater. Chem. A 5 (2017) 2123–2131, https://doi.org/10.1039/c6ta09378g.

[13] U. Kang, S.K. Choi, D.J. Ham, S.M. Ji, W. Choi, D.S. Han, A. Abdel-Wahab, H. Park, Photosynthesis of formate from CO$_2$ and water at 1% energy efficiency via copper iron oxide catalysis, Energy Environ. Sci. 8 (9) (2015) 2638–2643, https://doi.org/10.1039/C5EE01410G.

[14] Y.Y. Ahn, S.Y. Yang, C. Choi, W. Choi, S. Kim, H. Park, Electrocatalytic activities of Sb-SnO$_2$ and Bi-TiO$_2$ anodes for water treatment: Effects of electrocatalyst composition and electrolyte, Catal. Today 282 (2017) 57–64, https://doi.org/10.1016/j.cattod.2016.03.011.

[15] G. Kim, H.J. Choi, H.-i. Kim, J. Kim, D. Monllor-Satoca, M. Kim, H. Park, Temperature-boosted photocatalytic H$_2$ production and charge transfer kinetics on TiO$_2$ under UV and visible light, Photochem. Photobiol. Sci. 15 (10) (2016) 1247–1253, https://doi.org/10.1039/C6PP00263C.

[16] S. Kim, G.-H. Moon, G. Kim, U. Kang, H. Park, W. Choi, TiO$_2$ complexed with dopamine-derived polymers and the visible light photocatalytic activities for water pollutants, J. Catal. 346 (2017) 92–100, https://doi.org/10.1016/j.jcat.2016.11.027.

[17] V. Kumaravel, S. Rhatigan, S. Mathew, J. Bartlett, M. Nolan, S.J. Hinder, P.K. Sharma, A. Singh, J.A. Byrne, J. Harrison, S.C. Pillai, Indium-doped TiO$_2$ photocatalysts with high-temperature anatase stability, J. Phys. Chem. C 123 (34) (2019) 21083–21096, https://doi.org/10.1021/acs.jpcc.9b06811.

[18] M. Tahir, N.S. Amin, Indium-doped TiO$_2$ nanoparticles for photocatalytic CO$_2$ reduction with H$_2$O vapors to CH$_4$, Appl. Catal. B 162 (2015) 98–109, https://doi.org/10.1016/j.apcatb.2014.06.037.

[19] M. Tahir, N.S. Amin, Photocatalytic CO_2 reduction and kinetic study over In/TiO_2 nanoparticles supported microchannel monolith photoreactor, Appl. Catal. A 467 (2013) 483–496, https://doi.org/10.1016/j.apcata.2013.07.056.

[20] X. Li, R. Shen, S. Ma, X. Chen, J. Xie, Graphene-based heterojunction photocatalysts, Appl. Surf. Sci. 430 (2018) 53–107, https://doi.org/10.1016/j.apsusc.2017.08.194.

[21] M.M. Kandy, Carbon-based photocatalysts for enhanced photocatalytic reduction of CO_2 to solar fuels, Sustain. Energ. Fuels 4 (2) (2020) 469–484, https://doi.org/10.1039/C9SE00827F.

[22] S. Ye, R. Wang, M.-Z. Wu, Y.-P. Yuan, A review on g-C_3N_4 for photocatalytic water splitting and CO_2 reduction, Appl. Surf. Sci. 358 (2015) 15–27, https://doi.org/10.1016/j.apsusc.2015.08.173.

[23] J. Theerthagiri, R.A. Senthil, A. Priya, J. Madhavan, R.J.V. Michael, M. Ashokkumar, Photocatalytic and photoelectrochemical studies of visible-light active α-Fe_2O_3–g-C_3N_4 nanocomposites, RSC Adv. 4 (72) (2014) 38222–38229, https://doi.org/10.1039/C4RA04266B.

[24] J. Ran, W. Guo, H. Wang, B. Zhu, J. Yu, S.-Z. Qiao, Metal-free 2D/2D phosphorene/g-C_3N_4 Van der Waals heterojunction for highly enhanced visible-light photocatalytic H_2 production, Adv. Mater. 30 (25) (2018) 1800128, https://doi.org/10.1002/adma.201800128.

[25] S.C. Yan, Z.S. Li, Z.G. Zou, Photodegradation performance of g-C_3N_4 fabricated by directly heating melamine, Langmuir 25 (17) (2009) 10397–10401, https://doi.org/10.1021/la900923z.

[26] H.W. Jeong, W.-S. Chae, B. Song, C.-H. Cho, S.-H. Baek, Y. Park, H. Park, Optical resonance and charge transfer behavior on patterned WO_3 microdisc arrays, Energy Environ. Sci. 9 (2016) 3143–3150, https://doi.org/10.1039/C6EE01003B.

[27] S. Kim, H. Park, Sunlight-harnessing and storing heterojunction TiO_2/Al_2O_3/WO_3 electrodes for night-time applications, RSC Adv. 3 (2013) 17551–17558, https://doi.org/10.1039/C3RA42644K.

[28] H. Park, H.-H. Ou, U. Kang, J. Choi, M.R. Hoffmann, Photocatalytic conversion of carbon dioxide to methane on TiO_2/CdS in aqueous isopropanol solution, Catal. Today 266 (2016) 153–159, https://doi.org/10.1016/j.cattod.2015.09.017.

[29] J. Qiu, Y.i. Feng, X. Zhang, X. Zhang, M. Jia, J. Yao, Facile stir-dried preparation of g-C_3N_4/TiO_2 homogeneous composites with enhanced photocatalytic activity, RSC Adv. 7 (2017) 10668–10674, https://doi.org/10.1039/C7RA00050B.

[30] A.K. Nayak, S. Lee, Y. Sohn, D. Pradhan, Biomolecule-assisted synthesis of In(OH)$_3$ nanocubes and In_2O_3 nanoparticles: photocatalytic degradation of organic contaminants and CO oxidation, Nanotechnology 26 (48) (2015) 485601, https://doi.org/10.1088/0957-4484/26/48/485601.

[31] J. Ma, C. Wang, H. He, Enhanced photocatalytic oxidation of NO over g-C_3N_4-TiO_2 under UV and visible light, Appl. Catal. B 184 (2016) 28–34, https://doi.org/10.1016/j.apcatb.2015.11.013.

[32] X. Li, Z. Zhuang, W. Li, H. Pan, Photocatalytic reduction of CO_2 over noble metal-loaded and nitrogen-doped mesoporous TiO_2, Appl. Catal. A 429–430 (2012) 31–38, https://doi.org/10.1016/j.apcata.2012.04.001.

[33] L.-L. Tan, W.-J. Ong, S.-P. Chai, B.T. Goh, A.R. Mohamed, Visible-light-active oxygen-rich TiO_2 decorated 2D graphene oxide with enhanced photocatalytic activity toward carbon dioxide reduction, Appl. Catal. B 179 (2015) 160–170, https://doi.org/10.1016/j.apcatb.2015.05.024.

[34] X. Li, J. Zhang, L. Shen, Y. Ma, W. Lei, Q. Cui, G. Zou, Preparation and characterization of graphitic carbon nitride through pyrolysis of melamine, Appl. Phys. A-Mater 94 (2) (2009) 387–392, https://doi.org/10.1007/s00339-008-4816-4.

[35] E. Wang, W. Yang, Y. Cao, Unique surface chemical species on indium doped TiO_2 and their effect on the visible light photocatalytic activity, J. Phys. Chem. C 113 (49) (2009) 20912–20917, https://doi.org/10.1021/jp9041793.

[36] N. Cao, Z. Chen, K. Zang, J. Xu, J. Zhong, J. Luo, X. Xu, G. Zheng, Doping strain induced bi-Ti^{3+} pairs for efficient N_2 activation and electrocatalytic fixation, Nat. Commun. 10 (2019) 1–12, https://doi.org/10.1038/s41467-019-10888-5.

[37] B. Tahir, M. Tahir, N.S. Amin, Gold–indium modified TiO_2 nanocatalysts for photocatalytic CO_2 reduction with H_2 as reductant in a monolith photoreactor, Appl. Surf. Sci. 338 (2015) 1–14, https://doi.org/10.1016/j.apsusc.2015.02.126.

[38] D.C. Sorescu, W.A. Al-Saidi, K.D. Jordan, CO_2 adsorption on TiO_2 (101) anatase: a diserpsion-corrected density functional theory study, J. Chem. Phys. 135 (2011), 124701, https://doi.org/10.1063/1.3638181.

[39] K. Bhattacharyya, A. Danon, B.K. Vijayan, K.A. Gray, P.C. Stair, E. Weitz, Role of the surface Lewis acid and base sites in the adsorption of CO_2 on titania nanotubes and platinized titania nanotubes: an in situ FT-IR study, J. Phys. Chem. C 117 (24) (2013) 12661–12678, https://doi.org/10.1021/jp402979m.

[40] G.K. Ramesha, J.F. Brennecke, P.V. Kamat, Origin of catlaytic effect in the reduction of CO_2 at nanostructured TiO_2 films, ACS Catal. 4 (2014) 3249–3254, https://doi.org/10.1021/cs500730w.

[41] L. Tan, J. Xu, X. Zhang, Z. Hang, Y. Jia, S. Wang, Synthesis of g-C_3N_4/CeO_2 nanocomposites with improved catalytic activity on the thermal decomposition of ammonium perchlorate, Appl. Surf. Sci. 356 (2015) 447–453, https://doi.org/10.1016/j.apsusc.2015.08.078.

[42] B. Tahir, M. Tahir, N.A.S. Amin, Photo-induced CO_2 reduction by CH_4/H_2O to fuels over Cu-modified g-C_3N_4 nanorods under simulated solar energy, Appl. Surf. Sci. 419 (2017) 875–885, https://doi.org/10.1016/j.apsusc.2017.05.117.

[43] L. Kong, X. Zhang, C. Wang, J. Xu, X. Du, L. Li, Ti^{3+} defect mediated g-C_3N_4/TiO_2 Z-scheme system for enhanced photocatalytic redox performance, Appl. Surf. Sci. 448 (2018) 288–296, https://doi.org/10.1016/j.apsusc.2018.04.011.

[44] B. Zhu, P. Xia, Y. Li, W. Ho, J. Yu, Fabrication and photocatalytic activity enhanced mechanism of direct Z-scheme g-C_3N_4/Ag-$_2WO_4$ photocatalyst, Appl. Surf. Sci. 391 (2017) 175–183, https://doi.org/10.1016/j.apsusc.2016.07.104.

[45] G. Khan, Y.K. Kim, S.K. Choi, D.S. Han, A. Abdel-Wahab, H. Park, Evaluating the catalytic effects of carbon materials on the photocatalytic reduction and oxidation reactions of TiO_2, Bull. Korean Chem. Soc. 34 (4) (2013) 1137–1144, https://doi.org/10.5012/bkcs.2013.34.4.1137.

[46] S.K. Choi, S. Kim, S.K. Lim, H. Park, Photocatalytic comparison of TiO_2 nanoparticles and electrospun TiO_2 nanofibers: effects of mesoporosity and interparticle charge transfer, J. Phys. Chem. A 114 (39) (2010) 16475–16480, https://doi.org/10.1021/jp104317x.

[47] H. Wang, H. Li, Z. Chen, J. Li, X. Li, P. Huo, Q. Wang, TiO_2 modified g-C_3N_4 with enhanced photocatalytic CO_2 reduction performance, Solid State Sci. 100 (2020) 106099, https://doi.org/10.1016/j.solidstatesciences.2019.106099.

[48] Y.-N. Liu, C.-C. Shen, N. Jiang, Z.-W. Zhao, X. Zhou, S.-J. Zhao, A.-W. Xu, g-C_3N_4 hydrogen-bonding viologen for significantly enhanced visible-light photocatalytic H_2 evolution, ACS Catal. 7 (12) (2017) 8228–8234, https://doi.org/10.1021/acscatal.7b03266.

[49] H.L. Huynh, J. Zhu, G. Zhang, Y. Shen, W.M. Tucho, Y. Ding, Z. Yu, Promoting effect of Fe on supported Ni catalysts in CO_2 methanation by in situ DRIFTS and DFT study, J. Catal. 392 (2020) 266–277, https://doi.org/10.1016/j.jcat.2020.10.018.

[50] F. He, S. Weon, W. Jeon, M.W. Chung, W. Choi, Self-wetting triphase photocatalysis for effective and selective removal of hydrophilic volatile organic compound in air, Nat. Commun. 12 (2021) 6259, https://doi.org/10.1038/s41467-021-26541-z.

[51] L. Wang, W. Si, Y. Tong, F. Hou, D. Pergolesi, J. Hou, T. Lippert, S.X. Dou, J. i. Liang, Graphitic carbon nitride (g-C_3N_4)-based nanosized heteroarrays: Promising materials for photoelectrochemical water splitting, Carbon Energy 2 2 (2) (2020) 223–250, https://doi.org/10.1002/cey2.48.

[52] L. Mino, G. Spoto, A.M. Ferrari, CO_2 capture by TiO_2 anatase surfaces: a combined DFT and FTIR study, J. Phys. Chem. C 118 (43) (2014) 25016–25026, https://doi.org/10.1021/jp507443k.

[53] S. Huygh, A. Bogaerts, E.C. Neyts, How oxygen vacancies activate CO_2 dissociation on TiO_2 anatase (001), J. Phys. Chem. C 120 (38) (2016) 21659–21669, https://doi.org/10.1021/acs.jpcc.6b07459.

[54] B. Zhu, L. Zhang, D. Xu, B. Cheng, J. Yu, Adsorption investigation of CO_2 on g-C_3N_4 surfavce by DFT calculation, J. CO2 Util. 21 (2017) 327–335, https://doi.org/10.1016/j.jcou.2017.07.021.

[55] C.-C. Yang, Y.-H. Yu, B. van der Linden, J.C.S. Wu, G. Mul, Artificial photosynthesis over crystalline TiO_2-based catalysts: Fact or fiction? J. Am. Chem. Soc. 132 (24) (2010) 8398–8406, https://doi.org/10.1021/ja101318k.

[56] S.H. Yoon, U. Kang, H. Park, A. Abdel-Wahab, D.S. Han, Computational density functional theory study on the selective conversion of CO_2 to formate on homogeneously and heterogeneously mixed $CuFeO_2$ and CuO surfaces, Catal. Today 335 (2019) 345–353, https://doi.org/10.1016/j.cattod.2018.12.043.

[57] P. Wardman, Reduction potentials of one-electron couples involving free radicals in aqueous solution, J. Phys. Chem. Ref. Data 18 (4) (1989) 1637–1755, https://doi.org/10.1063/1.555843.